06

Zero-, one-, and two-dimensional modes in the Lugiato–Lefever model with focused pumps: A brief review

© B.A. Malomed

Department of Physical Electronics, School of Electrical Engineering, Faculty of Engineering, and the Center for Light-Matter University, Tel Aviv University,
Tel Aviv, Israel

e-mail: malomed@tauex.tau.ac.il

Received May 25, 2024
Revised May 25, 2024
Accepted July 29, 2024

A review is presented for theoretical results demonstrating the creation of stable spatially confined 0D (zero-dimensional), 1D, and 2D modes in the framework of the Lugiato-Lefever (LL) equations, which are fundamental models of externally driven nonlinear passive optical cavities. The confinement is imposed, in the 2D setting, by the tight harmonic-oscillator (HO) potential, or, in the framework of the 1D and 2D LL equations, by the tightly focused 1D or 2D pump term. The 2D modes, which are strongly confined by the HO potential, and driven by the zero-vorticity or vortical pump, realize effectively 0D pixels, with the respective vorticity. These solutions are obtained by means of the perturbation theory (in the 1D case), variational approximation (VA) and Thomas-Fermi approximation, as well as in the numerical form. The 1D LL equation with the tightly focused pump, which is approximated by the delta-function, gives rise to an exact solution of the codimension-one (non-generic) type, provided that the equation includes a cubic loss term, along with the linear one. In addition to the codimension-one analytical solution, generic ones are obtained in the numerical form, featuring shapes which are close to those of the analytical solution. These 1D modes are completely stable. The 2D LL equation including the focused pump with vorticity $S = 0, 1, 2, \ldots$, produces pump-pinned modes, that are found by means of VA and numerically. Stability regions are identified for these modes in the system's parameter space. Under the action of the self-focusing cubic nonlinearity, those vortex modes which are unstable spontaneously transform into necklace-shaped states. On the other hand, the defocusing nonlinearity maintains stability of the vortex modes, at least, up to $S = 5$.

Keywords: laser cavity; focused pump; localized modes; vortices; stability; variational approximation; Thomas-Fermi approximation; perturbation theory.

DOI: 10.61011/EOS.2024.08.60025.6736-24

1. Introduction

Equations of the Lugiato-Lefever (LL) type are commonly known as dynamical models for nonlinear passive optical cavities, with the intrinsic loss compensated by a pump term, which represents an external laser beam driving the cavity [1]. These models provide solutions for fundamental phenomena in laser optics, such as cavity solitons [2–6], chimera modes [7], switching waves [8], vortices [9,10], frequency combs [11–18], optical rogue waves [22–24], and self-trapped spatiotemporal modes [25].

In the properly scaled form, the LL equation for local complex amplitude $\phi(x, y.t)$ of the amplitude of the optical field trapped in the two-dimensional (2D) pumped lossy cavity with coordinates (x, y) and scaled time t is [1,26,27]

$$i\left(\gamma+\frac{\partial}{\partial t}\right)\phi=\left[-\frac{1}{2}\left(\frac{\partial^2}{\partial x^2}+\frac{\partial^2}{\partial y^2}\right)+\Delta + U(x,y)+\sigma|\phi|^2\right]\phi+E(x,y), \quad (1)$$

where $\gamma > 0$ is the loss coefficient, $E(x, y)$ represents the pump field, which in most cases is considered as the uniform one ($E = \text{const}$), but it may also be a localized function of the coordinates, if the pump is provided by a tightly focused laser beam [28–31], $\Delta \gtrless 0$ is the detuning of the pump with respect to the cavity, and effective potential $U(x, y)$ may be realized by spatial modulation $\delta n(x, y)$ of the local refractive index in the optical cavity, so that $U(x, y) \sim -\delta n(x, y)$. Further, the Laplacian in Eq. (1) represents the paraxial diffraction (in the scaled form), while $\sigma < 0$ and $\sigma > 0$ correspond, severally, to the self-focusing or defocusing cubic nonlinearity of the optical material. By means of additional rescaling applied to Eq. (1) one may fix $\gamma \equiv 1$, which is set below.

A relevant possibility is to consider the 2D LL equation with the pump provided by a laser beam with embedded vorticity (winding number) $m = \pm 1, \pm 2 \ldots$. The natural form of the vortex beam close to its pivot is written, in polar coordinates (r, θ), as

$$E = E_0 r^{|m|} e^{im\theta} \quad (2)$$

with $E_0 = \text{const}$ [28]. Naturally, the vortex beam supports vortical solutions of the LL equation with the same winding number m, while $m = 0$ corresponds to the fundamental modes.

A characteristic of the confined field is its total power (or norm, mathematically speaking),

$$P = \int\int |\phi(x,y,t)|^2 dxdy \tag{3}$$

(this definition implies that the integral converges). A simple corollary of Eq. (1) is the evolution equation for the power,

$$\frac{dP}{dt} = -2\gamma P - 2\int\int \mathrm{Im}\{E^*(x,y)\,\phi(x,y,t)\}dxdy, \tag{4}$$

where $*$ stands for the complex conjugate.

An important feature of physically relevant equations is a possibility to represent them in a Lagrangian form (see, e.g., Refs. [32] and [33]). Equation (1) in its usual form cannot be derived from a Lagrangian, as it includes the dissipative term, $\gamma\partial\phi/\partial t$. Nevertheless, the well-known substitution [34],

$$\phi(x,y,t) \equiv \Phi(x,y,t)\exp(-\gamma t), \tag{5}$$

eliminates it, introducing, instead, time-dependent coefficients in the LL equation:

$$i\frac{\partial}{\partial t}\Phi = \left[-\frac{1}{2}\left(\frac{\partial^2}{\partial x^2}+\frac{\partial^2}{\partial y^2}\right)+\Delta + U(x,y) + \sigma e^{-2\gamma t}|\Phi|^2\right]\Phi + E(x,y)\,e^{\gamma t}. \tag{6}$$

Unlike the underlying equation (1), the transformed one (6) can be derived from a real time-dependent Lagrangian [28,35],

$$L = \int\int dxdy\left\{\frac{i}{2}\left(\Phi_t^*\Phi - \Phi^*\Phi_t\right) + \frac{1}{2}\left(|\Phi_x|^2+|\Phi_y|^2\right) + \left[\Delta + U(x,y)\right]|\Phi|^2 + \frac{\sigma}{2}e^{-2\gamma t}|\Phi|^4 + e^{\gamma t}\left(E(x,y)\,\Phi^* + E^*(x,y)\,\Phi\right)\right\}. \tag{7}$$

The availability of the Lagrangian representation for the LL equation is an essential asset, making it possible to apply the variational approximation (VA), and thus to obtain important results in an approximate analytical form [28,29,31,32,35]. The one-dimensional (1D) version of the LL equation and the respective equations (4) and (7) are obtained by dropping coordinate y in the above equations, keeping only x in them.

The objective of the present article is to produce a concise review of previously obtained theoretical (analytical and numerical) findings for the 1D and 2D LL equations which maintain spatially confined states, either under the action of a localized pump, or imposing the localization by a strongly confining potential $U(x.y)$. The presentation chiefly follows original works [28,29,31], with the results for the zero-, one-, and two-dimensional LL equations reported in Sections 2, 3, and 4, respectively ("zero-dimensional" pertains to the 2D LL equation with a tightly confining potential, that effectively reduces the dynamics to that of a *pixel* [39,40], i.e., a point-like object.

In addition to that, it is relevant to mention that recent work [30] addressed localized modes maintained by the tightly focused pump in the 1D LL equation with the usual diffraction term replaced by its *fractional* counterpart,

$$-\partial^2/\partial x^2 \rightarrow \left(-\partial^2/\partial x^2\right)^{\alpha/2}, \tag{8}$$

where α, taking values $1<\alpha<2$, is the fractional Lévy index [36–38], which defines the fractional pseudodifferential operator (8) as the *Riesz derivative* [41],

$$-\frac{\partial^2}{\partial x^2}\phi = \frac{1}{2\pi}\int_{-\infty}^{+\infty}dp|p|^\alpha\int_{-\infty}^{+\infty}d\xi e^{ip(x-\xi)}\phi(\xi). \tag{9}$$

The analysis reported in Ref. [30] has identified shapes of localized modes pinned to the focused pump, and their stability domains, in the framework of the 1D fractional LL equation.

The article is completed by briefly formulated conclusions in Section 6.

2. Fundamental and vortical modes („zero-dimensional"ones) produced by the LL equation with the tightly confining potential

The effectively 0D pixel is modeled by Eq. (1) with spatially uniform pump, $E=$ const, and tightly confining harmonic-oscillator (HO) potential,

$$U_{\mathrm{HO}}(x,y) = \left(\Omega^2/2\right)\left(x^2+y^2\right). \tag{10}$$

Large strength Ω^2 of the HO potential (10) determines an effective radius of the pixel, as the HO radius in the Schrödinger equation with the potential (10), *viz.*, $r_{\mathrm{HO}} = 1/\sqrt{\Omega}$. The asymptotic form of the respective stationary solution of Eq. (1) at $r\rightarrow\infty$ is

$$\phi(r) \approx -\frac{2E}{(\Omega r)^2} + \frac{4(\Delta - i\gamma)E}{(\Omega r)^4}. \tag{11}$$

In this section, following Ref. [28], analytical approximations are presented first, *viz.*, the VA for the zero-vorticity fundamental modes, and the Thomas-Fermi approximation (TFA), which is relevant for vortex modes. This is followed by a summary of numerical results for both fundamental (zero-vorticity) and vortex pixel states. In particular, the numerical results are compared to the analytical predictions.

2.1. The variational approximation (VA) for the zero-vorticity (fundamental) modes

Proceeding to the VA, Eq. (11) suggests one to adopt the following variational *ansatz* for the optical amplitude $\Phi(x,y,t)$, which is the solution of Eq. (6) (recall this equation admits the variational representation based on Lagrangian (7)) [28]:

$$\Phi(x,y,t)=\epsilon\frac{f(t)\,e^{\gamma t+i\chi(t)}}{1+r^2 f(t)\,e^{i\chi(t)}}\,, \tag{12}$$

$$\epsilon\equiv-\frac{2E}{\Omega^2}\,, \tag{13}$$

where $f(t)$ and $\chi(t)$ are real variables (variational parameters). Note that the integral power (3) of the ansatz is

$$P=\frac{4\pi E^2 f}{\Omega^4}\frac{\chi}{\sin\chi}. \tag{14}$$

The substitution of ansatz (12) in Eq. (7) and the integration, $\iint dxdy$, produces, after simple manipulations [28], the following VA Lagrangian,

$$\frac{e^{-2\gamma t}}{\pi\epsilon^2}L_{\mathrm{VA}}=\frac{1}{2}f q_1(\chi)\frac{d\chi}{dt}-\frac{1}{2}q_2(\chi)\sin\chi\frac{df}{dt}+f^2q_2(\chi)$$
$$+\Delta f q_1(\chi)+\frac{\sigma\epsilon^2}{8}f^3q_3(\chi)-\Omega^2q_1(\chi)\cos\chi$$
$$-\frac{\Omega^2}{4}\int d\chi[q_3(\chi)\sin\chi]\,, \tag{15}$$

where $q_1(\chi)\equiv\chi/\sin\chi$, $q_2(\chi)\equiv[(\sin\chi-\chi\cos\chi)\,/\sin^3\chi$, and $q_3(\chi)\equiv[2\chi-\sin(2\chi)]/\sin^3\chi$.

The variation of the respective action, $\int L_{\mathrm{VA}}dt$, with respect to variables $f(t)$ and $\chi(t)$, produces the Euler-Lagrange equations [28]:

$$\frac{1}{2}\left[q_2(\chi)\cos\chi+q_2'(\chi)\sin\chi+q_1(\chi)\right]\frac{df}{dt}$$
$$+\left(\gamma f-\Omega^2\sin\chi\right)q_1(\chi)+\left(\Omega^2\cos\chi-\Delta f\right)q_1'(\chi)$$
$$-f^2q_2'(\chi)-\frac{g}{8}f^3q_3'(\chi)+\frac{\Omega^2}{4}q_3(\chi)\sin\chi=0\,, \tag{16}$$

$$\Delta\cdot q_1(\chi)+2fq_2(\chi)+\frac{3g}{8}f^2q_3(\chi)+\gamma q_2(\chi)\sin\chi$$
$$+\frac{1}{2}\left[q_2(\chi)\cos\chi+q_2'(\chi)\sin\chi+q_1(\chi)\right]\frac{d\chi}{dt}=0\,, \tag{17}$$

where (see Eq. (13))

$$g=\sigma\epsilon^2\equiv4\sigma E^2/\Omega^4. \tag{18}$$

While it may seem that Eqs. (16) and (17) are singular at $\chi=0$, a simple analysis demonstrates that all the singularities cancel, while a singularity is indeed possible at $\chi=\pi$.

First of all, stationary (fixed-point, FP) solutions of Eqs. (16) and (17), with $df/dt=d\chi/dt=0$, are determined by the system of equations

$$\left(\Omega^2\sin\chi-\gamma f\right)q_1(\chi)+\left(\Delta f-\Omega^2\cos\chi\right)q_1'(\chi)$$
$$+f^2q_2'(\chi)+\frac{g}{8}f^3q_3'(\chi)-\frac{\Omega^2}{4}q_3(\chi)\sin\chi=0, \tag{19}$$

$$\Delta q_1(\chi)+2fq_2(\chi)+\frac{3g}{8}f^2q_3(\chi)+\gamma q_2(\chi)\sin\chi=0, \tag{20}$$

where the $q'_{1,2,3}\equiv dq_{1,2,3}/d\chi$. It is easy to find approximate solutions of Eqs. (19) and (20), assuming that they have $|\chi|\ll\pi$ (see Eq. (12)). Then, in the lowest approximation, which takes into regard the condition of the strong confinement (large Ω^2 in potential (10)), Eqs. (20) and (19) produce explicit approximate solutions:

$$f\approx\frac{-2\pm\sqrt{4-18g\Delta}}{3g}, \tag{21}$$

$$\chi\approx\frac{\gamma\left(-2\pm\sqrt{4-18g\Delta}\right)}{g\Omega^2}, \tag{22}$$

which exist under condition $g\Delta<2/9$ (note that it always holds for $\Delta<0$).

Another approximate solution of Eqs. (19) and (20) can be found for large values of detuning Δ, provided that $g\Delta$ is negative (see Eq. (18)):

$$f\approx\sqrt{-2\Delta/g}-2/(3g)\,, \tag{23}$$

$$\chi\approx(15/2)\gamma/\Delta. \tag{24}$$

In the general case, the FP solutions of Eqs. (19) and (20), where, as said above, one may fix $\gamma\equiv1$, depend on three parameters: $\Delta\gtrless0$, $g\gtrless0$, and $\Omega^2>0$.

In addition to finding the FPs, the full dynamical version of the VA, represented by Eqs. (16) and (17), can be used to analyze stability of the FPs, as well as to predict the evolution of unstable states. In reality, such a dynamical analysis turns out to be very cumbersome, while direct numerical simulations are actually more efficient [28].

The predictions of the VA for the stationary states are compared to numerical solution below in Figs. 1 and 2, demonstrating, in most cases, good accuracy of the VA method.

2.2. The Thomas-Fermi approximation (TFA)

Patterns supported by the combination of trapping potential (10) and vortex pump (2) are looked for as solutions to the stationary version of Eq. (1) with the same integer vorticity m as in the pump:

$$\phi(r,\theta)=e^{im\theta}A(r), \tag{25}$$

where complex amplitude function A satisfies the radial equation.

$$\left[\frac{1}{2}\left(\frac{d^2}{dr^2}+\frac{1}{r}\frac{d}{dr}-\frac{m^2}{r^2}\right)-\Delta\right.$$
$$\left.+i\gamma-\frac{\Omega^2}{2}r^2-\sigma|A|^2\right]A=E_0r^{|m|}. \tag{26}$$

With the structure of the vortex pump defined as per Eq. (2), Eq. (26) produces localized vortex modes only for $m=0$ and ±1.

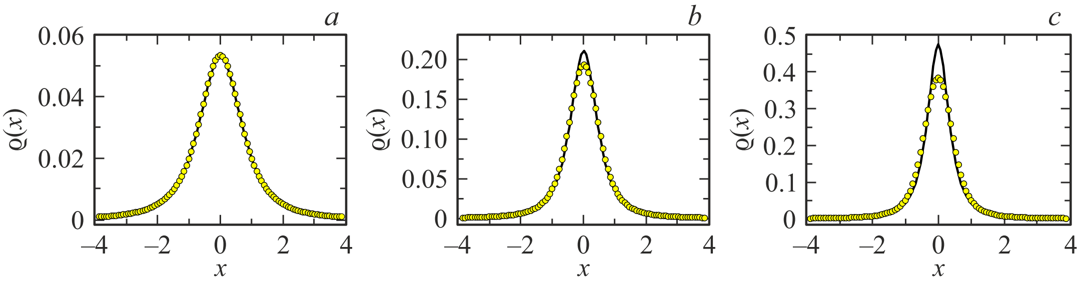

Figure 1. Profiles of trapped fundamental modes, $\varrho(x)$ (see Eq. (30)), obtained in Ref. [28] by dint of the imaginary-time simulations of the 2D equation (1), are shown by chains of yellow circles. Black solid lines are counterparts of the same profiles produced by the VA based on ansatz (12) and Eqs. (21) and (22). The mismatch values are (*a*) $\Delta = -1$, (*b*) $\Delta = -4$, (*c*) $\Delta = -10$, with other parameters fixed as $\Omega^2 = 100$, $\gamma = 1$, $E = 10$, and $g = 1$ (the self-defocusing sign of the nonlinearity, see Eq. (18)).

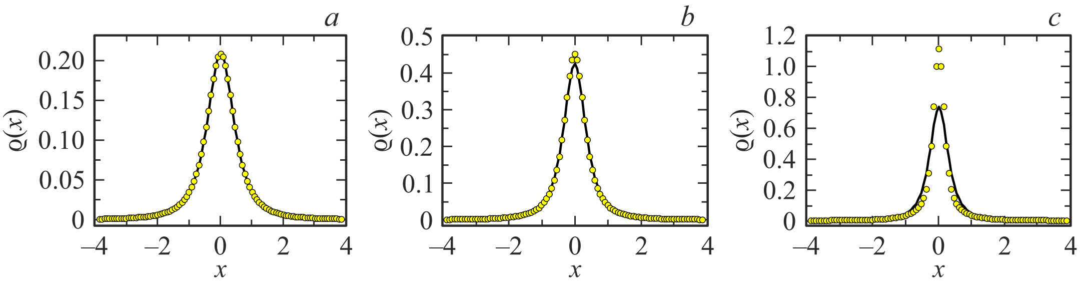

Figure 2. The same as in Fig. 1, but for (*a*) $\Delta = 1$, (*b*) $\Delta = 4$, (*c*) $\Delta = 10$, with $\Omega^2 = 100$, $\gamma = 1$, $E = 10$, and $g = -1$ (the self-focusing nonlinearity).

The TFA for vortex solitons may be applied here, cf. Ref. [43]. This approximation implies dropping the radial derivatives in Eq. (26), which leads to a complex cubic equation for amplitude A, which is relevant for $\sigma > 0$ (the self-defocusing sign of the cubic nonlinearity) and $\Delta > 0$ (positive mismatch in Eq. (1)):

$$\left[\Delta - i\gamma + \frac{1}{2}\left(\frac{m^2}{r^2} + \Omega^2 r^2\right) + \sigma |A|^2\right] A = -E_0 r^{|m|} . \quad (27)$$

Equation (27) strongly simplifies in the limit of large $\Delta > 0$, when both the imaginary and and nonlinear terms may be omitted:

$$A(r) = -E_0 r^{|m|} \left[\Delta + \frac{1}{2}\left(\frac{m^2}{r^2} + \Omega^2 r^2\right)\right]^{-1} . \quad (28)$$

For $|m| = 1$, Eq. (28) produces the ring-shaped vortex mode, with the maximal intensity located at

$$r^2_{\max} = \left(\sqrt{\Delta^2 + 3\Omega^2} + \Delta\right) / \Omega^2. \quad (29)$$

Recall that the TFA represented by Eqs. (27)–(29) is relevant only for $m = 0$ and $m^2 = 1$. For $m = 0$, the TFA-predicted profiles of the trapped modes are compared below to their numerically found counterparts in Fig. 3. For $m^2 = 1$, the comparison of values given by Eq. (29) with their counterparts extracted from numerically found vortex-ring shapes (see, e.g., Fig. 6 below), demonstrates that the approximate analytical values of $r^2_{\max}$, as given by Eq. (29), are smaller than the numerical ones by 11% for $\Delta = 0$, and by 6% for $\Delta = 10$ [28]. As expected, the TFA provides better accuracy for large Δ, but even for $\Delta = 0$ the prediction may be qualitatively correct.

2.3. Numerical results for zero-vorticity (fundamental) modes

2.3.1. Shapes of the stationary modes Localized fundamental-mode solutions to Eq. (1), with the confining potential (10) and constant pump E, were found in Ref. [28] by means of the well-known imaginary-time propagation method [44,45]. The initial guess for the numerical solution was chosen as per the VA ansatz (12), with f and χ taken according to Eqs. (21) and (22).

In Fig. 1, three typical examples of the 2D fundamental modes, produced by the numerical solution, are presented by their 1D integrated intensity profiles,

$$\varrho(x) \equiv \int_{-\infty}^{+\infty} |\phi(x, y)|^2 dy, \quad (30)$$

along with their analytically predicted VA counterparts, based on ansatz (12) and simplified variational equations (21) and (22), for three different values of detuning Δ: (a) $\Delta = -1$, (b) $\Delta = -4$, and (c) $\Delta = -10$, for $g = 1$ (the self-defocusing nonlinearity, see Eq. (18)), large confinement strength, $\Omega^2 = 100$, and the pump strength $E = 10$.

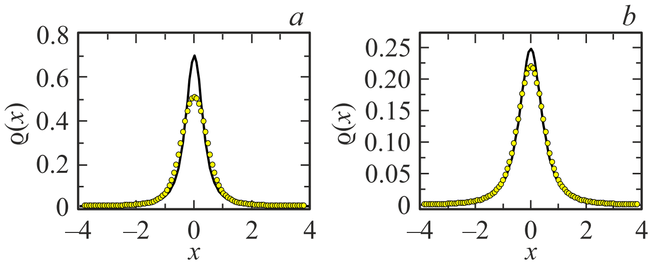

Figure 3. Similar to Figs. 1 and 2, chains of yellow circles represent profiles of the fundamental modes, $\varrho(x)$, obtained in Ref. [28] from the imaginary-time solution of Eq. (1), for the self-defocusing nonlinearity, $g = 1$, and large positive values of the mismatch: $\Delta = 10$ (a) and $\Delta = 20$ (b). Black solid lines display analytical counterparts of the same profiles, produced by the TFA as per Eq. (31). Other parameters are $\Omega^2 = 100$, $\gamma = 1$, and $E = 10$.

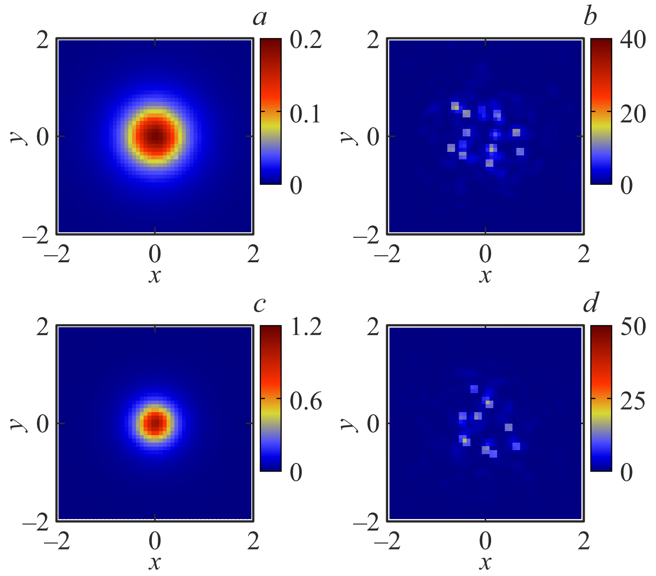

Figure 4. The strong instability of the fundamental mode produced (in Ref. [28]) by the simulations of Eq. (1) with the self-focusing nonlinearity ($\sigma = -1$). Panels (a, b) and (c, d) pertain to values of the mismatch $\Delta = 1$ and $\Delta = 10$, respectively. The other parameters are $E = 10$, $\Omega^2 = 100$, and $\gamma = 1$. Panels (a,c) and (b,d) display, severally, the input at $t = 0$ and output at $t = 10$.

Similar results obtained for the self-focusing nonlinearity (with $g = -1$, see Eq. (18)) and three positive values of the mismatch, *viz.*, (a) $\Delta = 1$, (b) $\Delta = 4$, and (c) $\Delta = 10$, with the same fixed values $\Omega^2 = 100$ and $E = 10$ as in Fig. 1, and displayed in Fig. 2. For both the self-defocusing and focusing signs of the nonlinearity, $g = \pm 1$, the VA profiles demonstrate good accuracy in comparison to their numerical counterparts.

Figure 3 exhibits typical profiles of the fundamental modes in the case when the TFA applies, *viz.*, the nonlinearity is defocusing and mismatch Δ takes large positive values. In particular, the integrated intensity profile produced by the substitution of the TFA solution (28) with $m = 0$ in definition (30) is

$$\varrho_{\mathrm{TFA}}(x) = \frac{2\pi E^2}{\Omega^4}\left(\frac{2\Delta}{\Omega^2} + x^2\right)^{-3/2}. \qquad (31)$$

Figure 3 corroborates that the TFA is quite accurate in the range of its applicability.

2.3.2. Stability of the fundamental modes The stability of the fundamental modes was tested in Ref. [28] by means of real-time simulations of Eq. (1), adding 5% random noise to the input and using the well-established split-step algorithm [46]. The systematic simulations were performed using the input predicted by the VA based on ansatz (12) and simplified variational equations (21) and (22). In fact, the difference of the VA-predicted shape from its numerically predicted counterpart was an additional initial perturbation, which helps one to test the stability of the fundamental modes.

First, the simulations demonstrate the stability of the fundamental modes in the case of the self-defocusing, $\sigma = +1$ in Eq. (1): the perturbed input quickly relaxes towards the stationary fundamental mode (sometimes exhibiting persistent oscillations around it, with a relatively small amplitude, see details in Ref. [28]). A similar outcome of the perturbed evolution was observed in the case of the self-focusing, with $\sigma = -1$, and sufficiently large positive values of mismatch Δ. The latter finding is qualitatively explained by the fact that the lossless unpumped limit of the 2D LL equation (1), with $\gamma = E = 0$, $\sigma = -1$, and the trapping HO potential (10), i.e., the 2D nonlinear Schrödinger equation (NLS) with the HO potential term and cubic self-focusing, admits a completely stable family of fundamental solitons, with the negative chemical potential, which corresponds to $\Delta > 0$, in terms of Eq. (1) [47].

On the other hand, at some other values of parameters, Eq. (1) with the self-focusing sign, $\sigma = -1$, gives rise to strong instability of the fundamental modes through fast fragmentation, as shown in Fig. 4. This dynamical regime may be considered as a manifestation of the modulational instability in the LL equation, driven by the cubic self-focusing [11,26]. Further, the large size of local amplitudes in small spots, which is demonstrated by the development of the instability in Fig. 4, implies the trend towards the onset of the 2D *critical collapse* driven by the self-focusing cubic term [48,49].

The existence and stability of the localized fundamental modes produced by Eq. (1) with the confining HO potential (10) are summarized by charts displayed in Fig. 5 for three values of the strength of the HO potential: (a) $\Omega^2 = 4$, (b) $\Omega^2 = 16$, and (c) $\Omega^2 = 100$. The stability area is composed of gray and white boxes, which correspond, respectively, to static outcomes of the simulations, or those featuring small residual oscillations, on top of the stationary shapes. Unstable solutions were found in the area not covered by boxes. As mentioned above, the stability domain is the one of self-defocusing ($\sigma = +1$ in Eq. (1), and also a smaller domain of the self-focusing ($\sigma = -1$), combined with large positive values of mismatch Δ. In the stability areas shown in Fig. 5, black spots highlight values of the parameters at which the output profiles of the static solutions are very close to the input ones, i.e., the VA, even in the simplified form based on Eqs. (21) and (22) provides very accurate predictions.

Essentially the same stability charts which are displayed in Fig. 5 can be produced by (longer) simulations of Eq. (1) which start not from the VA ansatz, but simply from the zero input. This fact stresses the robustness of the eventual results.

2.4. Vortex states maintained by the tightly confining potential

The approximate analytical results for localized vortex modes supported by the combination of pump (2) with embedded vorticity $m = 1$ and tight confining potential (10) are produced by means of TFA, as shown above by Eqs. (25)−(29). Numerical results for stable vortex modes were produced in Ref. [28] by direct simulations of the respective equation (1), starting from the zero input. This simulation scenario is appropriate, as vortices, if they are stable, are strong attractors drawing solutions which develop from the zero.

A typical example of a stable ring-shaped vortex mode produced by Eq. (1) with the self-defocusing nonlinearity is displayed in Fig. 6. Unstable vortex modes suffer strong fragmentation, similar to the picture displayed above for the unstable fundamental modes in Fig. 4 (see details in Ref. [28]).

More complex stable vortex profiles were found too. As shown in Fig. 7, they feature a multi-ring radial structure, and a spiral shape of the phase distribution (note that this complex mode is, quite surprisingly, stable as the solution of Eq. (1) with the self-focusing nonlinearity). Actually, emerging spirality in the phase pattern can be seen in Fig. 6, *b* too. The spirality is explained by the fact that Eq. (26) produces amplitude $A(r)$ as a complex function, as seen in Eqs. (11) and (27). The spirality of vortex modes is a well-known feature of 2D complex Ginzburg-Landau (CGL) equations [50,51] (in which spatial patterns are maintained not by the pump field, but by the intrinsic gain), although in solutions of the CGL equation the phase spirality is not usually related to a multi-ring radial structure. The stability of the multi-ring patterns produced by the present version of the LL equation is a remarkable findings, as similar patterns tend to be completely unstable in many other models [53,54].

The results for the vortex modes are summarized in Fig. 8 by means of stability charts in the plane of the mismatch and nonlinearity strength, (Δ, σ), for $\Omega^2 = 4$ in Eq. (10) and $E_0 = 1$ or 2 in Eq. (2). Note that, for the self-focusing nonlinearity ($\sigma < 0$), the stability domain for the vortex modes is essentially larger than its counterpart in the chart for the fundamental (zero-vorticity) modes, cf. Fig. 5, which was also plotted for $\Omega^2 = 4$. This inference may be explained by the fact that the vanishing of the modal field $A(r)$ at $r \to 0$ (see Eq. (28)) makes the central area of the vortex mode nearly „empty“, thus preventing the occurrence of the modulational instability in it [28].

The gray and yellow areas in Fig. 8 are populated, severally, by the single- and multi-ring vortex structures, see examples in Figs. 6 and 7, respectively. Note that, in panel (*b*), the stable multi-ring modes are found solely for $\sigma = 0$, which implies the linearized version of the LL Eq. (1). On the other hand, in panel (b) they exist also at $\sigma \neq 0$ (as solutions of the nonlinear equation), provided that mismatch Δ takes negative values with sufficiently large $|\Delta|$. This observation is easily explained by the fact that the combination of the basic terms in Eq. (26) with $m = 1$ and $\Delta < 0$,

$$\left[\frac{1}{2}\left(\frac{d^2}{dr^2} + \frac{1}{r}\frac{d}{dr} - \frac{1}{r^2}\right) - \Delta\right] A, \tag{32}$$

is the same as in the usual Bessel equation, hence the multi-ring structures naturally correspond to the oscillatory shape of the standard Bessel function, $J_1\left(\sqrt{-2/\Delta}r\right)$.

3. One-dimensional localized modes maintained by the LL equation with a tightly focused pump

Localized 1D modes can be readily generated by the LL equation with a tightly focused pump, even in the absence of any confining potential. This possibility was investigated in Ref. [29] in the framework of the model represented by the following equation:

$$i\left(\gamma + \frac{\partial}{\partial t}\right)\phi = \left(-\frac{1}{2}\frac{\partial^2}{\partial x^2} + \Delta + \sigma|\phi|^2\right)\phi + E(x), \tag{33}$$

cf. its 2D counterpart (1). Similar to Eq. (1), $\sigma = -1$ and $+1$ define the self-focusing and defocusing sign of the cubic term, while the absolute value of the nonlinearity coefficient is fixed here as $|\sigma| = 1$.

Note that, while the usual form of the 1D LL equation (33) is written in the notation corresponding to a spatial laser cavity, the same equation with t replaced by the propagation distance, z, and coordinate x replaced by the reduced time, $\tau \equiv t - x/V_{\mathrm{gr}}$ (here V_{gr} is the group velocity of the carrier wave) provides a dynamical model of a passive fiber temporal-domain cavity, pumped by a copropagating optical wave, $E(\tau)$ [55]. In particular, the case of a tightly focused pump, considered in this section, corresponds to the pump wave represented by a temporal-domain soliton.

Stability of stationary modes produced by Eq. (33) may be enhanced if a cubic-loss term, represented by coefficient

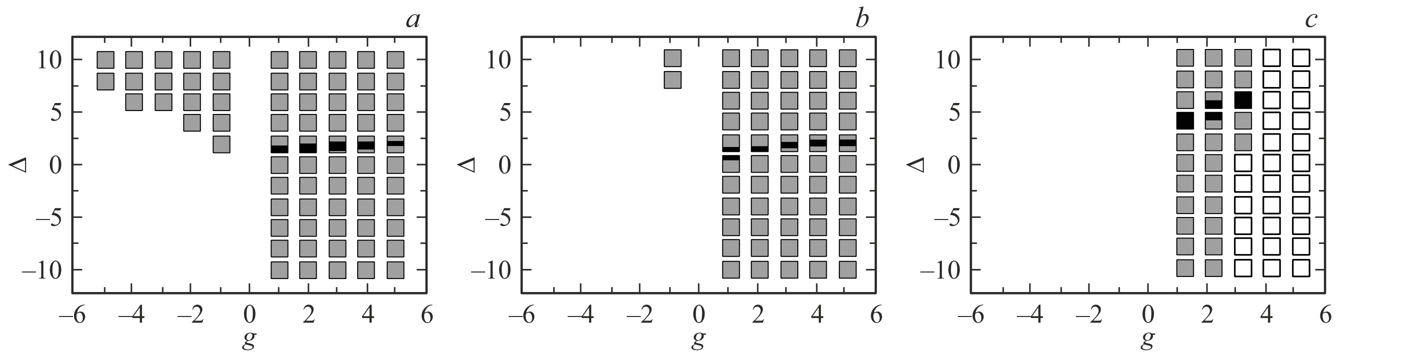

Figure 5. The existence area of stable fundamental modes produced (in Ref. [28]) by real-time simulation of Eq. (1). To generate the area, the input was used in the form of ansatz (12) with parameters predicted by the simplified VA equations (21) and (22), adding random noise at the 5% amplitude level. The three panels correspond to $\Omega = 2$ (a), $\Omega = 4$ (b), and $\Omega = 10$ (c). In gray boxes, the simulations quickly converge to stationary states, while in white boxes the stable modes keep small intrinsic oscillations. Instability, in the form of the fragmentation (see Figs. 4 (b) and 4 (d)), takes place in the area not covered by boxes. The results for the linear version of Eq. (1), corresponding to $g = 0$, are not included, as all the stationary solutions are obviously stable as solutions of the linear equation.

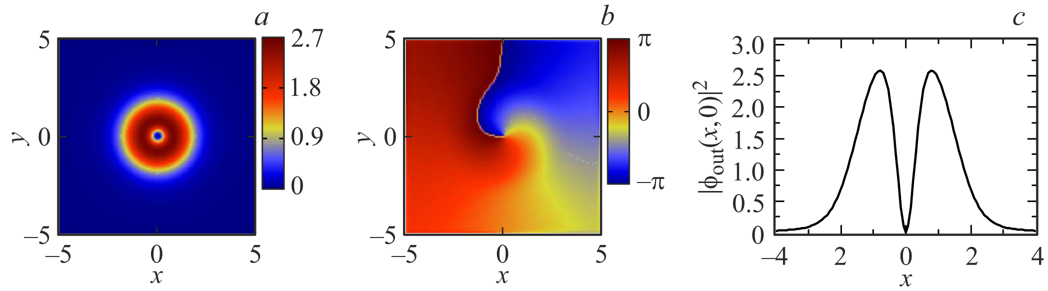

Figure 6. (a) Local-intensity $|\phi(x, y)|^2$ and (b) phase profiles of a stable vortex mode produced in Ref. [28] by the simulations of Eq. (1) with vortex pump (2) ($m = 1$) and confining potential (10). Panel (c) depicts the radial profile of the vortex mode along the cross section $y = 0$. Parameters are $\sigma = 2$ (the self-defocusing nonlinearity), $\Delta = -8$, $\gamma = 1$, $\Omega = 2$, and $E_0 = 1$.

$\Gamma > 0$, is added to the linear loss in Eq. (33):

$$i\left(\gamma + \Gamma|\phi|^2 + \frac{\partial}{\partial t}\right)\phi = \left(-\frac{1}{2}\frac{\partial^2}{\partial x^2} + \Delta + \sigma|\phi|^2\right)\phi + E(x). \quad (34)$$

The cubic loss term represents the effect of the two-photon absorption, if it takes place in the laser cavity.

3.1. The perturbative treatment of the 1D mode

In the case of the self-focusing nonlinearity and positive detuning ($\sigma = -1$ and $\Delta > 0$ in Eq. (33)), the perturbation theory was developed in Ref. [29], treating $i\gamma\phi$ and $E(x)$ as small terms. In the zero-order approximation, a localized solution is taken as the usual NLS soliton [56],

$$\phi(x) = e^{-i\xi}\,\sqrt{2\Delta}\,\mathrm{sech}\left(\sqrt{2\Delta}x\right). \quad (35)$$

The constant phase shift ξ in this approximation for the stationary mode is determined by the balance condition for the integral power,

$$P = \int_{-\infty}^{+\infty} |\phi(x)|^2\,dx, \quad (36)$$

which is the 1D version of definition (3). Indeed, it follows from the power-balance condition, $dP/dt = 0$, as produced by Eq. (34), that the 1D stationary solution must satisfy the integral condition

$$\gamma P + \Gamma\int_{-\infty}^{+\infty} |\phi(x)|^4\,dx = -\int_{-\infty}^{+\infty} E(x)\mathrm{Im}\left\{\phi(x)\right\}dx \quad (37)$$

(cf. its 2D counterpart following from Eq. (4)). The substitution of approximation (35) in Eq. (37) predicts the value of the phase shift:

$$\sin\xi = \frac{2\left[\gamma + (4/3)\,\Gamma\Delta\right]}{\int_{-\infty}^{+\infty} E(x)\,\mathrm{sech}\left(\sqrt{2\Delta}x\right)dx}. \quad (38)$$

Note that, even for the weak delocalized pump, $E(x) = \mathrm{const} \equiv \mathscr{E}_0$, with small $\mathscr{E}_0$, integral $\int_{-\infty}^{+\infty} E(x)\mathrm{sech}\left(\sqrt{2\Delta}x\right)dx$ converges, hence the approximation based on Eqs. (35)–(38) predicts a

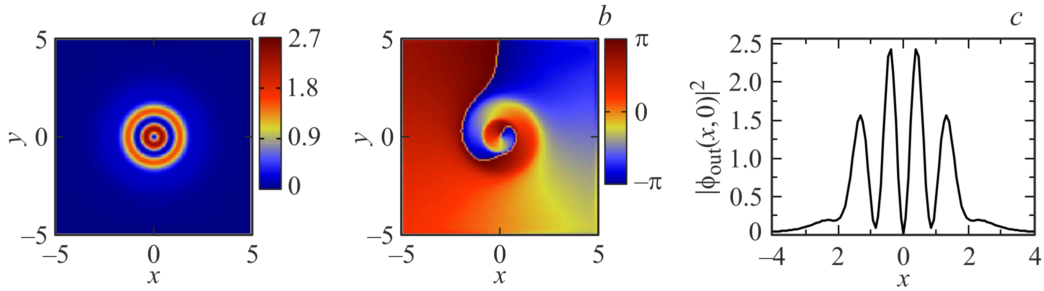

Figure 7. A stable multi-ring vortex with the spiral phase field, produced (in Ref. [28]) as the numerical solution of Eq. (1). Panels (a), (b), and (c) have the same meaning as in Fig. 6. Parameters are $\sigma = -1$ (the self-focusing nonlinearity), $\Delta = -8, \gamma = 1, \Omega^2 = 4$, and $E_0 = 1$.

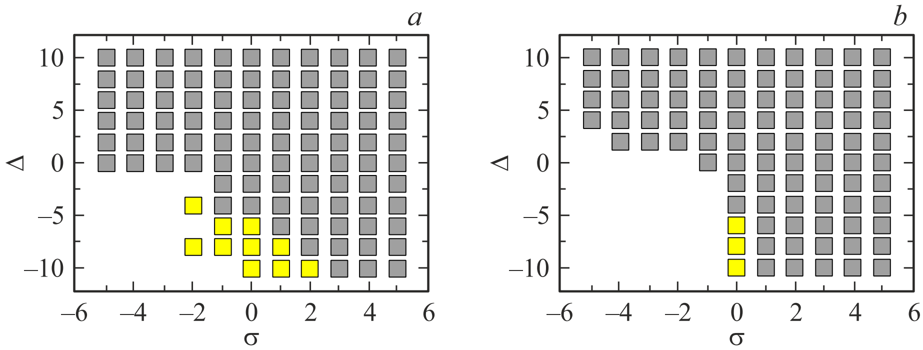

Figure 8. Stability areas in the plane of (Δ, σ) for the vortex modes numerically generated in Ref. [28] by the real-time simulations of Eq. (1) with the confining potential (10) and vortex pump (2) with winding number $m = 1$. Other parameters are $\gamma = 1$, $\Omega^2 = 4$, and $E_0 = 1$ in (a), or $E_0 = 2$ in (b). Stable single-ring vortices (see Fig. 6) are found in the gray areas, while the yellow ones are populated by stable multi-ring vortex modes with the spiral phase structure, see Fig. 7. No stable vortices were found in the white area.

localized mode created on top of a flat background, with a small amplitude $\phi_0 \approx \mathscr{E}_0/(\Delta + i\gamma)$, under the condition that the amplitude $\sqrt{2\Delta}$ of solution (35) is much larger than ϕ_0, i.e., $\mathscr{E}_0^2 \ll \Delta^3$ [29].

3.2. A particular exact solution and states close to it

The gain localized in a very narrow region may be approximated by the Dirac's delta-function,

$$E(x) = E_0\, \delta(x). \tag{39}$$

In this case, the homogeneous version of Eq. (34),

$$i\left(\gamma + \Gamma|\phi|^2 + \frac{\partial}{\partial t}\right)\phi = \left(-\frac{1}{2}\frac{\partial^2}{\partial x^2} + \Delta + \sigma|\phi|^2\right)\phi, \tag{40}$$

must be solved with the boundary condition at $x = 0$ determined by the integration of Eq. (34) with the pump term (39) in an infinitesimal vicinity of $x = 0$. The latter condition amounts to the jump of the first derivative at $x = 0$:

$$\frac{d\phi}{dx}|_{x=+0} - \frac{d\phi}{dx}|_{x=-0} = 2E_0. \tag{41}$$

An *exact solution* of Eq. (40) with the boundary condition (41) is [29]

$$\phi(x) = \frac{Ae^{i\xi}}{[\sinh(\lambda(|x| + \xi))]^{1+i\mu}}, \tag{42}$$

with parameters (μ is called the *chirp*)

$$\mu = -\gamma/\lambda^2, \tag{43}$$

$$A^2 = 3\gamma/(2\Gamma), \tag{44}$$

$$\lambda^2 = \frac{\gamma}{4\Gamma}\left(\sqrt{9\sigma^2 + 8\Gamma^2} + 3\sigma\right), \tag{45}$$

$$\xi = \frac{1}{2\lambda}\operatorname{arcosh}\left(1 + \frac{\chi}{E_0^2} + \sqrt{4 + \frac{\chi}{\lambda^2 E_0^4}}\right), \tag{46}$$

$$\zeta = \pi - \arctan\mu + \mu\ln(\sinh(\lambda\xi)), \tag{47}$$

where $\chi \equiv A^2\lambda^2(1 + \mu^2)$ and $\operatorname{arcosh}(Z) \equiv \ln\left(Z + \sqrt{Z^2 - 1}\right)$.

This exact solution is a non-generic one, as it exists at the *single value* of the mismatch parameter,

$$\Delta_0 = \frac{1}{2}\left(\frac{3\sigma\gamma}{\Gamma} - \lambda^2\right) \tag{48}$$

(in other words, it is a *codimension-one* type of the exact solution, with „one" referring to one constraint (48), which must be adopted to obtain the solution). The ingredient of the exact solution given by Eq. (45) is valid, giving $\lambda^2 > 0$, for both the focusing and defocusing signs of the nonlinearity, $\sigma = -1$ and $+1$.

Note that the presence of the cubic-loss term in Eq. (34), with $\Gamma > 0$, is necessary for the existence of the exact solution. Indeed, letting $\Gamma \to 0$ in Eq. (45) leads to a singular limit:

$$\lambda^2 \approx \begin{cases} 3\gamma/(2\Gamma) & \text{at} \quad \sigma = +1, \\ (1/3)\Gamma\gamma & \text{at} \quad \sigma = -1. \end{cases} \tag{49}$$

It is relevant to mention that exact solutions of the codimension-one type for the pinned states were found too in the 1D model based on the CGL equation with the delta-function gain (rather than pump). The difference is that the CGL equation with the localized gain also admits the zero state, which may or may not be stable [57].

3.3. Numerical results

In Ref. [29], numerical solution of Eq. (34) with the delta-function pump (39) was performed using the standard Gaussian approximation for the delta-function,

$$\widetilde{\delta}(x) = (\sqrt{\pi}w)^{-1}\exp(-x^2/w^2), \tag{50}$$

with a sufficiently small width w. On the other hand, if a discretized form of the LL equation, with a mesh size Δx, is used for the numerical solution, width w in Eq. (50) may not be too small in comparison to Δx. In fact, it was found that the numerical scheme was stable for $w > \Delta x/2$ [29].

With these approximations, numerical stationary solutions were produced by direct simulations of Eq. (34), starting from the zero input, $\phi(x, t = 0) = 0$. The output, to which the numerical solution relaxed, was categorized as a stable mode if it maintained a static profile for a long time, $t \sim 1000$, which corresponds to $\gtrsim 100$ characteristic diffraction times t_{diffr}. According to Eq. (34), this time scale for a mode of width Λ is estimated as $t_{\text{diffr}} \sim 2\Lambda^2$.

In Fig. 9, typical examples of the analytically found solutions for the modes pinned to the delta-function are plotted for the focusing and defocusing nonlinearities, i.e., for $\sigma = -1$ and $\sigma = +1$, respectively, along with their numerically found counterparts. In this case, the parameters of Eqs. (34) and (39) are set as $\gamma = \Gamma = E_0 = 1$, and the value of mismatch Δ is taken as per Eq. (48), i.e., $\Delta_0(\sigma = -1) \approx -1.64$, $\Delta_0(\sigma = +1) \approx 0.61$. The numerical solutions plotted in the same panels were produced for three different values of the width used in the regularized delta-function (50), *viz.*, $w = 0.05$, 0.10, and 0.15.

Because the codimension-one analytical solution, represented by Eqs. (42)–(47), is valid under constraint (48) imposed on the parameters, it is relevant to explore the *structural stability* of the pinned modes against deviations from this constraint. To this end, the analytical and numerical solutions found with the value of mismatch $\Delta = \Delta_0$, selected as per Eq. (48), and numerical solutions found for $\Delta = 0.75\Delta_0$ and $1.25\Delta_0$ are plotted in Fig. 10. It is seen that such considerable changes of Δ produce a weak effect, i.e., the solutions are structurally stable ones. In other words, the codimension-one analytical solution for the pinned mode adequately represents generic ones.

The solutions displayed in Figs. 9 and 10 for the self-defocusing and focusing signs of the nonlinearity ($\sigma = +1$ and -1, respectively) exhibit counter-intuitive features: the pinned modes are more tightly localized and have a larger amplitude in the self-defocusing case than in case of focusing. This feature is explained by the effect of the cubic loss term $\sim \Gamma$ in Eq. (34). Indeed, the shape of the modes is essentially affected by their chirp μ (see Eqs. (42) and (43)), which is generated by that term.

The results produced by the analytical solution for the pinned mode and its numerically found counterpart are summarized in Fig. 11, which displays the effect of the variation of the pump's amplitude E_0 (see Eq. (50)) and dissipation coefficient γ in Eq. (34) on the peak local power, $\max[|\phi|^2] \equiv |\phi(x = 0)|^2$, and integral power P (see Eq. (36)) of the analytical solution, given by Eqs. (42)–(47), and its numerically found counterparts. The results are displayed for both the defocusing ($\sigma = +1$) and focusing ($\sigma = -1$) signs of the cubic self-interaction. These plots are relevant for the realization of the model, as both the pump's strength E_0 and effective loss rate γ can be readily controlled in the experiment (in particular, γ can be adjusted as the difference between the background material loss and lasing gain in the cavity). Naturally, the powers gradually increase with the growth of E_0, and decay with the growth of γ.

Finally, systematic simulations of the perturbed evolution of the pinned modes, performed in the framework of Eqs. (34) and (39), corroborate the stability of all numerical solutions approximating the exact analytical one [29]. Furthermore, all the solutions were found to be strong *attractors*, to which the direct simulations Eq. (34) quickly relax, starting from the zero input, $\phi(x, t = 0) = 0$.

4. Two-dimensional localized modes maintained by the LL equation with a focused pump

4.1. The zero-vorticity pump

As a direct extension of the 1D LL equation (33), one can consider its 2D version with a focused pump term [29]:

$$i\left(\gamma + \frac{\partial}{\partial t}\right)\phi = \left[-\frac{1}{2}\left(\frac{\partial^2}{\partial x^2} + \frac{\partial^2}{\partial y^2}\right) + \Delta + \sigma|\phi|^2\right]\phi + E(x, y). \tag{51}$$

Here the cubic loss is not included ($\Gamma = 0$, cf. Eq. (33)), as, unlike the analytical 1D solution (42), this term is not

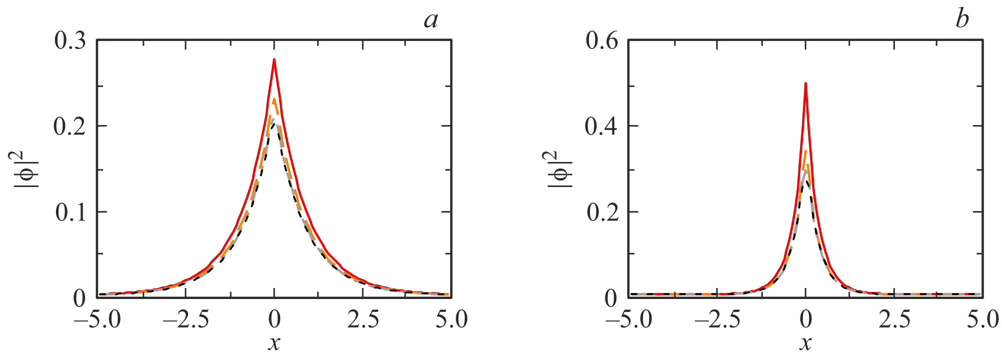

Figure 9. Solid red lines represent the exact solution (42) for the mode pinned to the delta-function pump, along with a set of numerical solutions based on the use of the regularized delta-function (50), with the finite width $w = 0.05$ (dashed orange lines), $w = 0.1$ (dashed-dotted gray lines), and $w = 0.15$ (dotted black lines). The results displayed in panels (*a*) and (*b*) pertain to the self-focusing ($\sigma = -1$) and self-defocusing ($\sigma = +1$) signs of the nonlinearity, respectively. Other parameters are $E_0 = \gamma = \Gamma = 1$, while Δ is given by Eq. (48). All the numerically found solutions are stable. The figure is borrowed from Ref. [29].

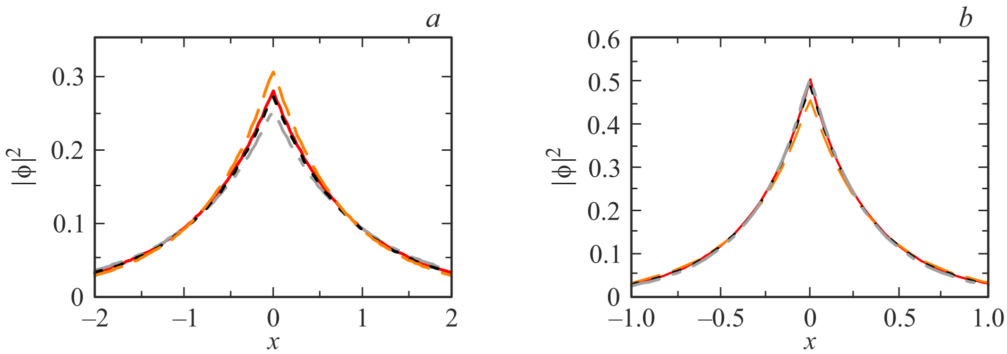

Figure 10. Solid red lines display the exact solution given by Eqs. (42)–(47) for the mode pinned to the delta-function pump (39). They are compared to a set of the numerically found solutions produced in Ref. [29] with the regularized delta-function (50). Dotted black lines pertain to the mismatch parameter $\Delta = \Delta_0$, taken exactly as per Eq. (48). Dashed orange lines and dashed-dotted gray ones correspond, respectively, to $\Delta = 0.75\Delta_0$ and $\Delta = 1.25\Delta_0$. The solutions displayed in panels (*a*) and (*b*) were obtained for the self-focusing ($\sigma = -1$) and defocusing ($\sigma = +1$) signs of the nonlinearity, respectively. Other parameters in Eq. (34) are $E_0 = \gamma = \Gamma = 1$. All numerical solutions displayed here are stable. The figure is borrowed from Ref. [29].

necessary for finding 2D numerical solutions considered here. Further, as mentioned above, one may fix the linear loss parameter, $\gamma \equiv 1$, by means of rescaling. A natural form of the tightly confined 2D pump term is the isotropic Gaussian with radius W,

$$E(x, y) = \frac{E_0}{\sqrt{\pi}W} \exp\left(-\frac{x^2 + y^2}{2W^2}\right), \qquad (52)$$

where $E_0 \equiv \int\int E(x, y)\, dxdy$ is the pump's integral intensity.

In the framework of VA (cf. its 1D version based on Eqs. (12)–(24)), approximate stationary solutions to Eq. (51) can be looked for in the form of the chirped Gaussian,

$$\phi(x, y) = A \exp\left[-(B - iC)\, r^2\right], \qquad (53)$$

where $r \equiv \sqrt{x^2 + y^2}$ is the radial coordinate, and amplitude A, squared inverse radial width $B > 0$, and chirp C are real variational parameters. Detailed analysis, reported in Ref. [29], leads to a cumbersome system of VA equations for them:

$$\sigma A^3 + \frac{\left[4B(B + \Delta) + 4C^2\right]}{2B} A + \frac{8WE_0B^2\left(1 + 2BW^2\right)}{\sqrt{\pi}\left[4B^3W^4 + 4B^2W^2 + (4W^4C^2 + 1)\, B\right]} = 0, \qquad (54)$$

$$\sigma BA^3 + 4\left(\Delta B + 2C^2\right) A + \frac{8W^3E_0B^3\left[1 + 4\left(B^2 - C^2\right) W^4 + 4BW^2\right]}{\sqrt{\pi}\left(1 + 4\left(B^2 + C^2\right) W^4 + 4BW^2\right)^2} = 0, \qquad (55)$$

$$\frac{\pi\,(2C - \gamma)\, A}{2B^2} - \frac{32W^5E_0\left(1 + 2BW^2\right) C}{\sqrt{\pi}\left[1 + 4\left(B^2 + C^2\right) W^4 + 4BW^2\right]^2} = 0. \qquad (56)$$

Typical examples of stable localized isotropic modes produced by Eqs. (51) and (52) in the variational and

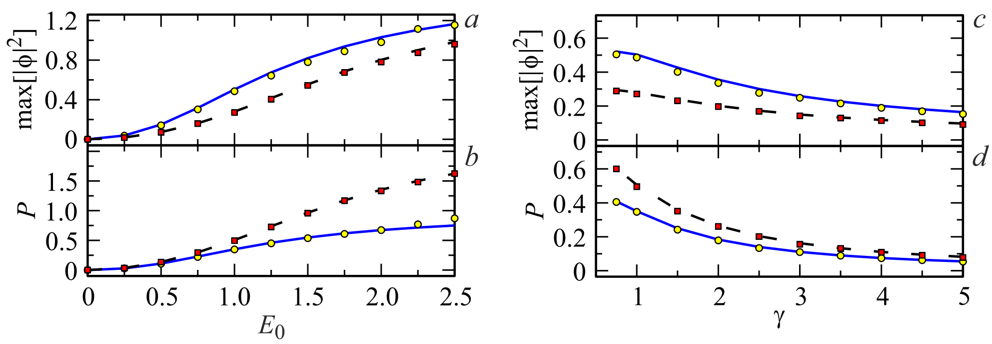

Figure 11. Panels (a, c) and (b, d) show the peak local power $\left(\max[|\phi|^2] \equiv |\phi\,(x=0)|^2\right)$ and integral norm (P, see Eq. (36)) as functions of the pump amplitude E_0 (see Eq. (50)) and linear-dissipation coefficient γ. In the left and right columns, coefficients are fixed, severally, as $\gamma = \Gamma = 1$ and $E_0 = \Gamma = 1$. In all panels, the data produced by the analytical solution for $\sigma = +1$ and -1, (the self-defocusing and focusing signs of the nonlinearity) are displayed by solid blue and dashed black lines, respectively. The corresponding results produced by the numerical solution are shown, severally, by chains of yellow circles and red boxes. The figure is borrowed from Ref. [29].

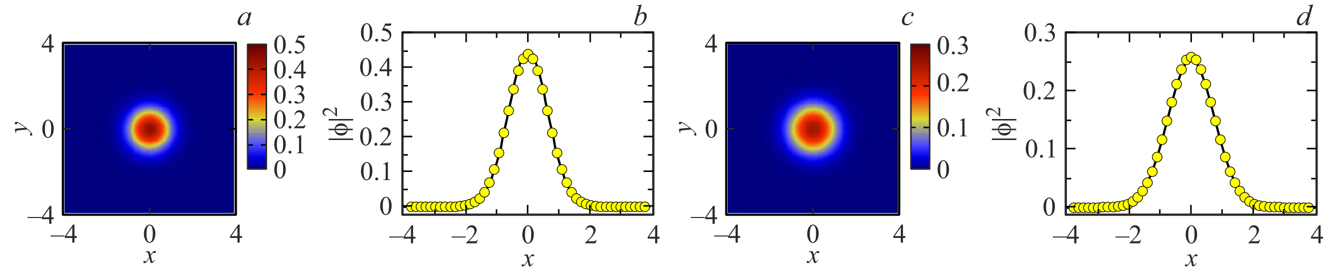

Figure 12. Typical profiles of stable 2D modes, $|\phi\,(x, y)\,|^2$, as produced in Ref. [29] by the numerical solution of Eq. (51) for $\Delta = -10$ (a) and $\Delta = 10$ (c). Cross-section profiles of the same modes, $|\phi(x, 0)|^2$, are displayed in panels (b) and (d), respectively. Lines in (b) and (d) represent the approximate analytical solution based on *ansatz* (53), chains of yellow circles representing the corresponding numerical solutions. Other parameters in Eqs. (51) and (52) are $E_0 = 10$ and $\sigma = \gamma = W = 1$.

numerically exact form are displayed in Fig. 12. It is seen that the VA may provide very accurate solutions in the quasi-analytical form.

In a small segment of their existence region (covered by yellow squares in the stability charts displayed in Fig. 14), numerically found stable 2D modes feature a crater-like shape, with the maximum of the local power located at a finite distance from the center, see an example in Fig. 13. Obviously, the analytical approximation based on the simple Gaussian *ansatz* (12) cannot reproduce this shape.

The most important results produced by the analysis of solutions of the 2D LL equation (51) with the confined zero-vorticity pump (52) are summarized in Fig. 14 by means of stability charts for the localized 2D modes in the plane of the mismatch and nonlinearity coefficients, (Δ, σ), for fixed pump's parameters, $E_0 = 10$ and $W = 1$. In this figure, which is borrowed from Ref. [29], red and yellow squares designate segments of the parameter plane which are populated, respectively, by the usual bell-shaped modes (see Fig. 12) and the crater-shaped ones (see Fig. 13). Further details of the analytical and numerical results for the 2D modes pinned to the localized zero-vorticity pump can be found in Ref. [29].

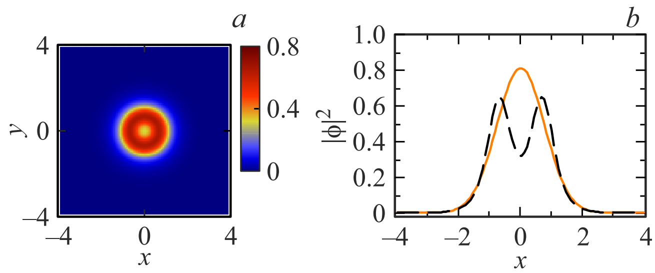

Figure 13. (a) The same as in Fig.12 (a), but for $\sigma = -5$ and $\Delta = -4$. (b) The black dashed line is the radial cross-section profile, $|\phi\,(x, 0)|^2$, of the numerically generated crater-shaped mode. The orange solid line shows a formal VA prediction for the same parameters.

4.2. Confined modes supported by the localized vortex pump

4.2.1. The definition of the model A natural possibility to extend the analysis of the 2D model, which was recently addressed in Ref. [31], is to consider localized pump with embedded vorticity $S \geq 1$ (similar to integer winding number m in Eq. (2)). Accordingly, the 2D LL

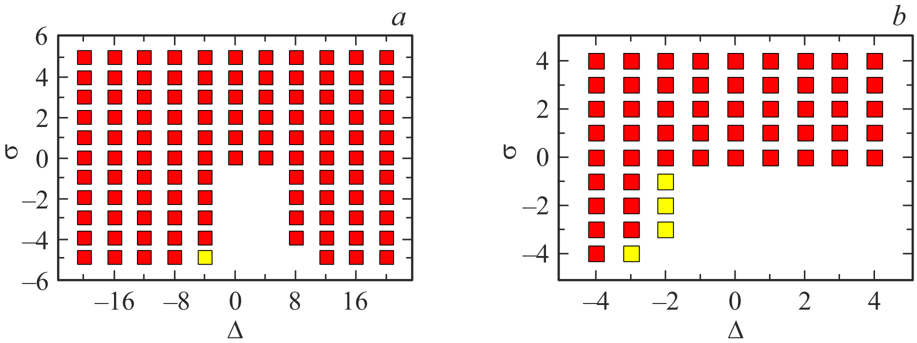

Figure 14. Stability charts for 2D localized isotropic modes in the plane of parameters (Δ, σ) (the mismatch and nonlinearity strength), as produced, in Ref. [29], by the numerical solution of Eqs. (51) and (52). Parameters of the pump are $E_0 = 10$ and $W = 1$. Panel (a) covers the range of $\sigma \in [-5, +5]$ and $\Delta \in [-20, +20]$, while (b) is a zoom of (a) for $\sigma \in [-4, +4]$ and $\Delta \in [-4, +4]$. The region covered by red boxes is populated by the bell-shaped) modes, such as the one plotted in Fig. 12. Yellow boxes designate a small segment of the parameter plane in which the stable isotropic modes is a crater-shaped, one, with the maximum of the local power located at a finite distance from the center, see an example in Fig. 13.

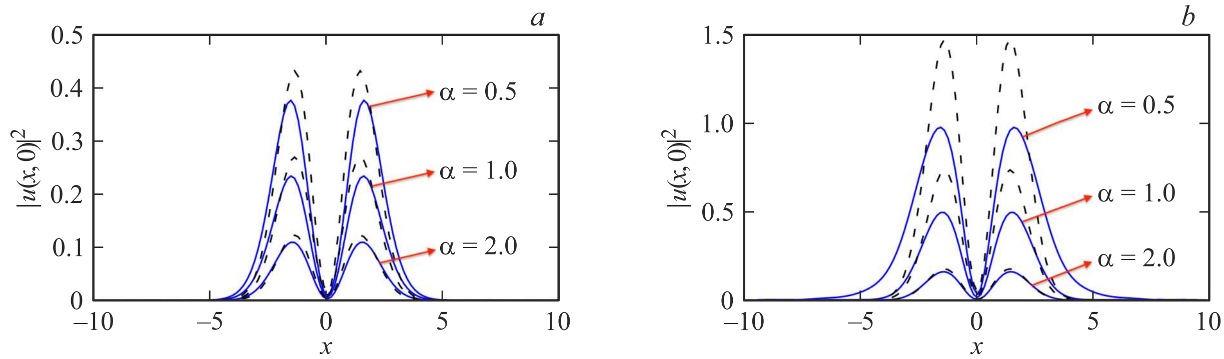

Figure 15. The comparison between cross-sections (drawn through $y = 0$) of the variational solutions for the vortex modes and their numerical counterparts (dashed black and solid blue lines, respectively) for different values of the loss parameter α in Eq. (57) belonging to the set (66). Panels (a) and (b) pertain, respectively, to the self-focusing $(\sigma = -1)$ and defocusing $(\sigma = +1)$ signs of cubic nonlinearity. Other parameters in Eqs. (57) and (58) are fixed as $\eta = f_0 = 1$, $W = 2$, and $S = 1$. All the vortex modes presented in this figure are stable. The figure is borrowed from Ref. [31].

equation (51) is replaced by the one written in the polar coordinates (r, θ):

$$i\left(\alpha + \frac{\partial}{\partial t}\right)u = -\frac{1}{2}\left(\frac{\partial^2}{\partial r^2} + \frac{1}{r}\frac{\partial}{\partial r} + \frac{1}{r^2}\frac{\partial}{\partial \theta^2}\right)u + \sigma\left(|u|^2 - \eta^2\right)u + E(r)e^{iS\theta}, \quad (57)$$

where notation u, instead of ϕ, is used for the optical field, the loss factor is denoted as α (instead of γ above), the mismatch is written as $\Delta \equiv \sigma\eta^2$, and the confined vortex pump with strength f_0 is taken as

$$E(r) = i f_0 r^m \exp\left(-r^2/W^2\right). \quad (58)$$

The difference from the vortex pump defined above in the form of expression (2) is that here it is necessary to introduce the radial confinement of the pump, with width W, once the confining potential is not included in Eq. (57). Pump vortex beams with a confined radial structure are used in diverse experimental setups [58].

Equation (57) is written in the scaled form. In physical units, $r = 1$ and $t = 1$ normally correspond to the spatial and time scales ~ 50 μm and ~ 50 ps, respectively, for a laser cavity. Then, the typical width $W = 2$, considered below, corresponds to the pump beam with waist ~ 100 μm, which is an experimentally relevant value. Accordingly, the characteristic evolution time in simulations presented below, $\dot{t} \sim 100$, corresponds to the physical time ~ 5 ns [31].

Stationary solutions of Eq. (57) are characterized by the total power, defined as in Eq. (3), and the angular momentum,

$$M = i\int_{-\infty}^{+\infty} dx \int_{-\infty}^{+\infty} dy u^* \left(y\partial_x u - x\partial_y u\right) dxdy, \quad (59)$$

with $*$ standing for the complex conjugate, even if the power and angular momentum are not dynamical invariants of the dissipative LL equation. In the case of stationary axisymmetric solutions with vorticity S, i.e., $u(x, y) = u(r)e^{iS\theta}$, the angular momentum is $M = SP$.

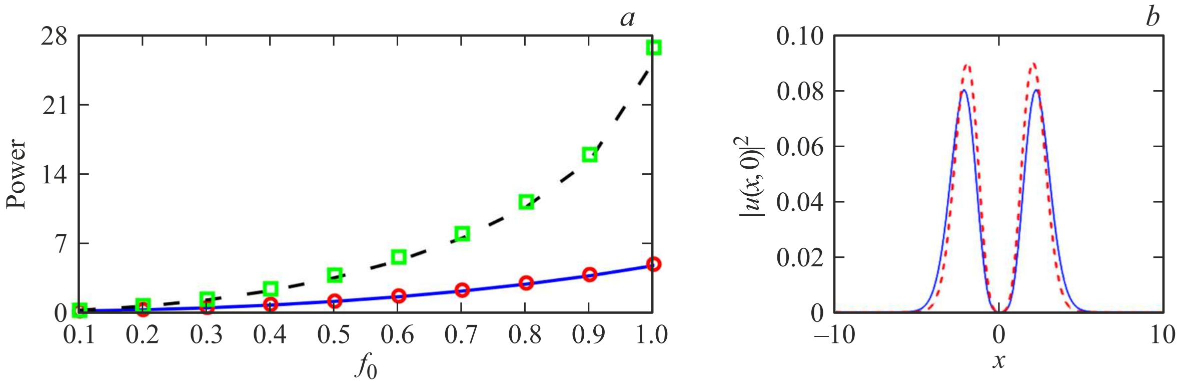

Figure 16. (a) The power of the localized vortex modes versus strength f_0 of the vortex pump in the self-focusing case ($\sigma = -1$ in Eq. (57)). The results produced for $S = 1$ and 2 by the quasi-analytical VA solutions, based on Eqs. (63) and (64), are shown by solid blue and dashed black lines, respectively. The corresponding numerical solutions are represented by red circles and green squares, respectively.The numerical solutions are stable, in this case, at $f_0 < 1.6$ and $f_0 < 1.1$ for $S = 1$ and 2, respectively, i.e., the plotted families are completely stable. (b) The VA-predicted and numerically obtained (dashed red and solid blue lines, respectively) profiles of the stable solution with $S = 2$ and $f_0 = 0.4$, drawn as cross-sections through $y = 0$. The other parameters are $\alpha = \eta = 1$ and $W = 2$.

4.2.2. Analytical considerations

First, the linearization of Eq. (57), with the pump substituted as per Eq. (58), straightforwardly produces the asymptotic expression for the tail of the vortex mode decaying at $r \to \infty$:

$$u(r,\theta) \approx (i/2)W^4 r^{S-2} \exp\left(-r^2/W^2 + iS\theta\right). \quad (60)$$

The global analytical approximation for the localized vortex modes is offered by VA based on the Gaussian ansatz

$$u(r,\theta) \equiv U(r)\exp(iS\theta) = U_0 r^S \exp\left(-\frac{r^2}{W^2} + iS\theta + i\phi\right), \quad (61)$$

where the variational parameters are the real amplitude U_0 of the solution and its phase shift ϕ from the pump. Power (3) of this ansatz is

$$P_S = \pi S! \left(W^2/2\right)^{S+1} U_0^2. \quad (62)$$

Note that the local power $|U(r)|^2$, corresponding to *ansatz* (61), which vanishes at $r \to 0$ and $r \to \infty$, attains its maximum at $r^2 = SW^2/2$.

The VA gives rise to the following equations for parameters ϕ and U_0:

$$\cos\phi = \alpha U_0/f_0, \quad (63)$$

$$2^{3S+1} S! \left\{ f_0 W^2 \sin\phi + \left[(S+1) - \sigma W^2\right] U_0 \right\} + (2S)!\sigma W^{2S+2} U_0^3 = 0. \quad (64)$$

Note that Eq. (63) is tantamount to the equation produced by the substitution of ansatz (61) in the power-balance condition following from Eq. (57) (cf. Eq. (37)):

$$2\pi \int_0^\infty f(r) \mathrm{Re}\left\{U(r,t)\right\} r dr = \alpha P. \quad (65)$$

The constraint $\cos\phi \le 1$ implies that, for the fixed pump's amplitude f_0, the amplitude of the localized vortex mode does not exceed the maximum value, which corresponds to $\phi = 0$ in Eq. (63), *viz.*, $U_0 \le (U_0)_{\max} = f_0/\alpha$.

4.2.3. Numerical results

Cross sections (drawn through $y = 0$) of the variational and numerical solutions for stable vortex modes obtained for values of the loss parameter

$$\alpha = 0.5,\ 1.0,\ 2.0, \quad (66)$$

are plotted for $\sigma = -1$ and $+1$ (the self-focusing and defocusing cubic nonlinearity) in Figs. 15(a) and (b), respectively, while the other coefficients in Eqs. (57) and (58) are fixed as $\eta = 1$, $f_0 = 1$, $W = 2$, and $S = 1$. It is seen that the VA accuracy improves with the increase of α, being essentially better for the self-focusing sign of the cubic nonlinearity. The larger discrepancy in the case of the self-defocusing is explained by the fact that localized modes (bright solitons) are not naturally maintained by the defocusing nonlinearity.

Families of stable vortex modes with $S = 1$ and 2 are presented by the corresponding $P(f_0)$ dependences plotted in Fig. 16(a) for the focusing sign of the nonlinearity in Eq. (57), i.e., $\sigma = -1$. These dependences are relevant for the realization of the predicted modes, as it is easy to vary the intensity of the pump beam, f_0^2, in the experiment.

In the case of the self-focusing sign of the nonlinearity ($\sigma = -1$) and fixed pump strength f_0, there is a critical value α_{crit} of the loss parameter α, so that at $\alpha < \alpha_{\text{crit}}$ the vortex solitons are unstable against spontaneous breaking of the axial symmetry. In particular, $\alpha_{\text{crit}} \approx 0.35$ for the values of the other parameters fixed as in Fig. 15(a). On the other hand, for $\sigma = -1$ and fixed α the instability of the vortex mode against the spontaneous breaking (splitting) sets in at $f_0 > (f_0)_{\text{crit}}$ (when the nonlinearity, determined by the mode's amplitude, is too strong). For $\alpha = \eta = 1$ and $W = 2$ (the same parameters as fixed in Fig. 16), the critical values of f_0 are $(f_0)_{\text{crit}}(S=1) \approx 1.6$, $(f_0)_{\text{crit}}(S=2) \approx 1.1$, $(f_0)_{\text{crit}}(S=3) \approx 0.6$, $(f_0)_{\text{crit}}(S=4) \approx 0.3$, and $(f_0)_{\text{crit}}(S=5) \approx 0.08$, respectively. Naturally, narrow

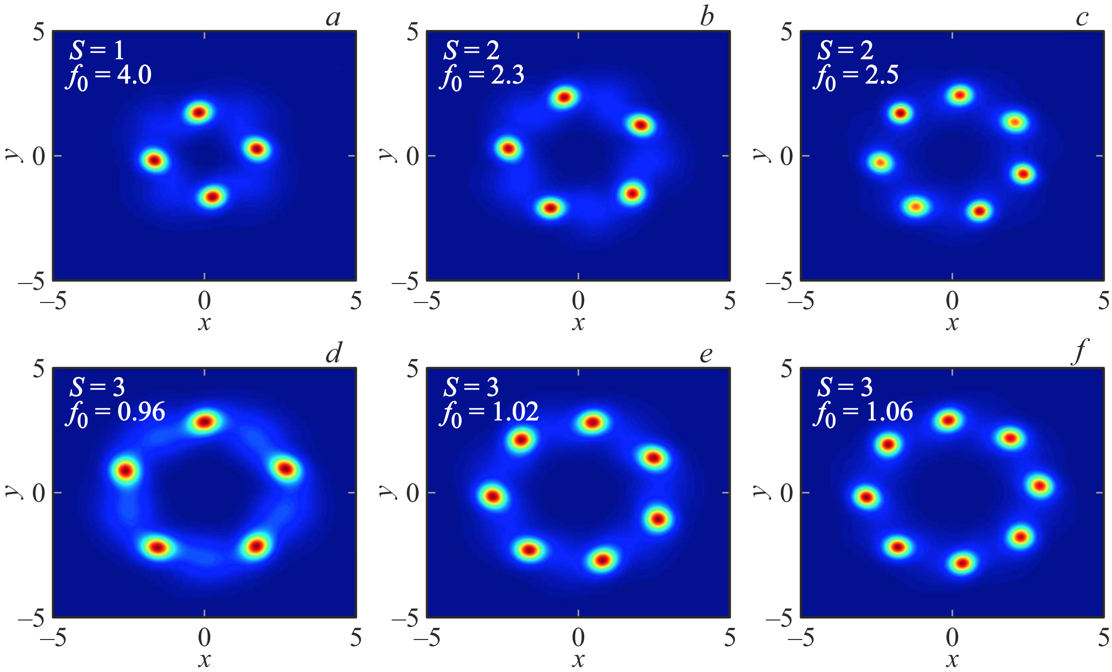

Figure 17. The fission of unstable vortex-ring modes into necklace-shaped structures, as demonstrated (in Ref. [31]) by simulations of Eqs. (57) and (58), with $\sigma = -1$ (cubic self-focusing), $\alpha = 2$, $\eta = 1$, and $W = 2$. Each plot displays the result of the numerical simulations at time $t = 100$. Values of the vorticity (winding number) and pump's strength are indicated in panels.

vortex rings with large values of S are much more vulnerable to the spontaneous splitting initiated by the azimuthal modulational instability of the vortex rings.

Deeper in the instability region of the vortex modes, i.e., at f_0 essentially exceeding the corresponding critical values $(f_0)_{\text{crit}}(S)$, the splitting instability initiates fission of the vortex rings into slowly rotating necklace-shaped structures, composed of N identical fragments with equal distances between them, which resembles the typical scenario of the splitting instability of vortex rings in the framework of the NLS equation [47]. However, unlike the case of the NLS equation, the emerging necklace does not expand, being essentially pinned to the maximum of the vortex pump (52), hence the radius of the necklace remains approximately the same as the radius of the underlying unstable vortex ring. In the examples displayed in Fig. 17 the necklaces built of $N = 4$, 5, 7, and 8 fragments are produced by the fission of the unstable rings with winding numbers $S = 1$, 2 or 3, 2 or 3, and 3, respectively.

On the other hand, in the framework of the LL equation (57) with the self-defocusing nonlinearity ($\sigma = +1$) and the vortex pump with winding numbers $1 \leq S \leq 5$ the vortex modes are completely stable [31] (vorticities with $S > 5$ were not considered). Indeed, the defocusing nonlinearity does not give rise to the above-mentioned azimuthal modulational instability which might lead to the fission of the vortex rings.

5. Conclusion

The objective of this article is to produce a brief survey of theoretical results for the creation of stable localized 0D (zero-dimensional), 1D, and 2D modes in the framework of the LL (Lugiato-Lefever) equations, with the 2D confinement imposed by the tight HO (harmonic-oscillator) potential, or by the spatially localized 1D or 2D pump term. In the former case, the 2D modes, strongly confined by the HO potential and supported by the zero-vorticity (fundamental) or vortical spatially unconfined pump, may be considered as effective 0D pixels (with embedded vorticity, in the case of the vortex pump). The corresponding fundamental and vortex solutions were obtained by means of the VA (variational approximation) and Thomas-Fermi approximation, respectively, as well as in the numerical form. The 1D LL equation, which includes the strongly localized pump, represented by the delta-function, and the cubic loss term (in addition to the linear one), gives rise to the exact solution of the codimension-one (non-generic) type. Along with the analytical non-generic solution, generic ones were obtained in the numerical form, featuring shapes which are quite close to those of the analytical solution. All such 1D modes pinned to the delta-function pump are stable. In the framework of the 2D LL equation with the localized pump carrying vorticity $S = 0, 1, 2, \ldots$ the modes pinned to the pump were found by means of the VA and in the numerical form, and their stability regions were identified. In the case of the self-focusing nonlinearity, strongly unstable modes in the form of vortex rings spontaneously split into necklace-shaped states, while the defocusing nonlinearity supports stable vortex rings up to $S = 5$, at least.

Not included in this review are results for localized modes produced by the 1D LL equation which combines the fractional diffraction, defined as per Eq. (9), self-focusing nonlinearity, and the focused pump. The findings for the fractional LL equation were recently reported in Ref. [30].

As an extension of the work summarized in this article, it may be interesting to study setups based on 1D and 2D LL equations with two or several spatially separated pumps — in particular, the ones with opposite signs in the 1D case, or 2D pumps with opposite vorticities, $\pm S$.

Acknowledgments

The results summarized in this brief review were chiefly reported in Refs. [28,29,31] and also in Ref. [30]. I thank coauthors of those works for valuable collaboration: W.B. Cardoso, M.C.P. dos Santos, S. Kumar, and L. Salasnich. The work on these topics was supported, in part, by the Israel Science Foundation through grant No. 1695/22.

References

[1] L.A. Lugiato, R. Lefever. Phys. Rev. Lett., **58**, 2209–2211 (1987).
[2] G.J. de Valcárcel, K. Staliunas. Phys. Rev. A, **87**, 043802 (2013).
[3] H. Taheri, A.A. Eftekhar, K. Wiesenfeld, A. Adibi. IEEE Photonics J., **7**, 2200309 (2015).
[4] M. Karpov, H. Guo, A. Kordts, V. Brasch, M.H. Pfeiffer, M. Zervas, M. Geiselmann, T.J. Kippenberg. Phys. Rev. Lett., **116**, 103902 (2016).
[5] P. Parra-Rivas, D. Gomila, P. Colet, L. Gelens. Eur. Phys. J. D, **71**, 198 (2017).
[6] X. Dong, C. Spiess, V.G. Bucklew, W.H. Renninger. Phys. Rev. Res., **3**, 033252 (2021).
[7] M.G. Clerc, M.A. Ferré, S. Coulibaly, R.G. Rojas, M. Tlidi. Opt. Lett., **42**, 2906–2909 (2017).
[8] B. Garbin, Y. Wang, S.G. Murdoch, G.-L. Oppo, S. Coen, M. Erkintalo. Eur. Phys. J. D, **71**, 240 (2017).
[9] Y.-Y. Wang, M.-M. Li, G.-Q. Zhou, Y. Fan, X.-J. Lai. Eur. Phys. J. Plus., **134**, 161 (2019).
[10] Q.-H. Cao, K.-L. Geng, B.-W. Zhu, Y.-Y. Wang, C.-Q. Dai. Chaos Sol. & Fract., **166**, 112895 (2023).
[11] S. Coen, H.G. Randle, T. Sylvestre, M. Erkintalo. Opt. Lett., **38**, 37–39 (2013).
[12] Y.K. Chembo, C.R. Menyuk. Phys. Rev. A, **87**, 053852 (2013).
[13] M.R.E. Lamont, Y. Okawachi, A.L. Gaeta. Opt. Lett., **38**, 3478–3481 (2013).
[14] C. Godey, I.V. Balakireva, A. Coillet, Y.K. Chembo. Phys. Rev. A, **89**, 063814 (2014).
[15] V.E. Lobanov, G. Lihachev, T.J. Kippenberg, M.L. Gorodetsky. Opt. Exp., **23**, 7713–7721 (2015).
[16] Q. Li, T.C. Briles, D.A. Westly, T.E. Drake, J.R. Stone, B.R. Ilic, S.A. Diddams, S.B. Papp, K. Srinivasan. Optica, **4**, 193–203 (2017).
[17] Y.V. Kartashov, O. Alexander, D.V. Skryabin. Opt. Express, **25**, 11550–11555 (2017).
[18] L.A. Lugiato, F. Prati, M.L. Gorodetsky, T. Kippenberg. Phil. Trans. R. Soc. A, **376**, 20180113 (2018).
[19] A. Coillet, I. Balakireva, R. Henriet, K. Saleh, L. Larger, J.M. Dudley, C.R. Menyuk, Y.M. Chembo. IEEE Photonics J., **5**, 6100409 (2013). https://doi.org/10.1109/JPHOT.2013.2277882.
[20] F. Copie, M. Conforti, A. Kudlinski, A. Mussot, S. Trillo. Phys. Rev. Lett., **116**, 143901 (2016).
[21] S.-W. Huang, J. Yang, S.-H. Yang, M. Yu, D.-L. Kwong, T. Zelevinsky, M. Jarrahi, C.W. Wong. Phys. Rev. X, **7**, 041002 (2017).
[22] M. Tlidi, K. Panajotov. Chaos, **27**, 013119 (2017).
[23] K. Panajotov, M.G. Clerc, M. Tlidi. Eur. Phys. J. D, **71**, 176 (2017).
[24] M. Tlidi, M. Taki. Adv. Opt. Photonics, **14**, 87–147 (2022).
[25] Y. Sun, P. Parra-Rivas, F. Mangini, S. Wabnitz. Chaos, Solitons & Fractals, **183**, 114870 (2024).
[26] T. Hansson, S. Wabnitz. Nanophotonics, **5**, 231–243 (2016).
[27] P. Parra-Rivas, E. Knobloch, L. Gelens, D. Gomila. IMA J. Appl. Math., **86**, 856–895 (2021).
[28] W.B. Cardoso, L. Salasnich, B.A. Malomed. Eur. Phys. J. D, **71**, 112 (2017).
[29] W.B. Cardoso, L. Salasnich, B.A. Malomed. Sci. Rep., **7**, 16876 (2017).
[30] S. He, B.A. Malomed, D. Mihalache, X. Peng, Y. He, D. Deng. Chaos, Solitons & Fractals, **173**, 113737 (2023).
[31] S. Kumar, W.B. Cardoso, B.A. Malomed. Symmetry, **16**, 470 (2024).
[32] B.A. Malomed. Prog. Opt., **43**, 71–193 (2002).
[33] K.Y. Bliokh, A.Y. Bekshaev, F. Nori. New J. Phys., **15**, 033026 (2013).
[34] R.K. Bullough, A.P. Fordy, S.V. Manakov. Phys. Lett. A, **91**, 98–100 (1982).
[35] A.B. Matsko, L. Maleki. Opt. Exp., **21**, 28862–28867 (2013).
[36] N. Laskin. Phys. Lett. A, **268**, 298–305 (2000).
[37] N. Laskin. *Fractional Quantum Mechanics* (World Scientific, Singapore, 2018).
[38] B. Mandelbrot. *The Fractal Geometry of Nature* (W.H. Freeman, New York, 1982).
[39] M. Brambilla, L.A. Lugiato, F. Prati, L. Spinelli, W.J. Firth. Phys. Rev. Lett., **79**, 2042 (1997).
[40] S. Barland, J.R. Tredicce, M. Brambilla, L.A. Lugiato, S. Balle, M. Giudici, T. Maggipinto, L. Spinelli, G. Tissoni, T. Knödl, M. Miller, R. Jäger. Nature, **419**, 699–702 (2002).
[41] M. Cai, C.P. Li. Fractional Calculus Appl. Anal., **305**, 287–301 (2019).
[42] L.P. Pitaevskii, S. Stringari. *Bose-Einstein Condensation* (Oxford University Press, Oxford, 2003).
[43] A.L. Fetter. Rev. Mod. Phys., **81**, 647 (2009).
[44] M.L. Chiofalo, S. Succi, M.P. Tosi. Phys. Rev. E, **62**, 7438 (2000).
[45] W.Z. Bao, Q. Du. SIAM J. Sci. Comp., **25**, 1674–1697 (2004).
[46] J. Yang. *Nonlinear waves in integrable and nonintegrable systems* (SIAM, Philadelphia, 2010).
[47] D. Mihalache, D. Mazilu, B.A. Malomed, F. Lederer. Phys. Rev. A, **73**, 043615 (2006).
[48] L. Bergé. Phys. Rep., **303**, 259 (1998).
[49] G. Fibich. *The Nonlinear Schrödinger Equation: Singular Solutions and Optical Collapse* (Springer: Heidelberg, 2015).

[50] T. Bohr, G. Huber, E. Ott. Physica D, **106**, 95 (1997).
[51] M. Gabbay, E. Ott, P.N. Guzdar. Physica D., **118**, 371 (1998).
[52] L.-C. Crasovan, B.A. Malomed, D. Mihalache. Phys. Rev. E, **63**, 016605 (2001).
[53] J. Atai, Y.J. Chen, J.M. Soto-Crespo. Phys. Rev. A, **49**, R3170-R3173 (1994).
[54] A. Dubietis, G. Tamosauskas, G. Fibich, B. Ilan. Opt. Lett., **29**, 1126–1128 (2004).
[55] P. Parra-Rivas, D. Gomila, M.A. Matías, S. Coen, L. Gelens. Phys. Rev. A, **89**, 043813 (2014).
[56] V.E. Zakharov, S.V. Manakov, S.P. Novikov, L.P. Pitaevskii. *Solitons: the Inverse Scattering Method* (Springer, 1984).
[57] C.-K. Lam, B.A. Malomed, K.W. Chow, P. Wai. European Phys. J. Special Topics, **173**, 233–243 (2009).
[58] A.S. Reyna, C.B. de Araújo. Adv. Opt. Phot. **9**, 720–774 (2017).